Article

Design of a Resonant Converter for a Regenerative Braking System Based on Ultracap Storage for Application in a Formula SAE Single-Seater Electric Racing Car

Alberto Dolara [1,*,†] **, Sonia Leva** [1,†] **, Giacomo Moretti** [1,†] **, Marco Mussetta** [1,*,†] **and Yales Romulo de Novaes** [2,†]

1 Dipartimento di Energia, Politecnico di Milano, 20133 Milano, Italy; sonia.leva@polimi.it (S.L.); giacomo1.moretti@mail.polimi.it (G.M.)
2 Power Electronics Laboratory, Universidade do Estado de Santa Catarina, Joinville, SC 89219-710, Brazil; yales.novaes@udesc.br
* Correspondence: alberto.dolara@polimi.it (A.D.); marco.mussetta@polimi.it (M.M.)
† These authors contributed equally to this work.

Abstract: Electric mobility can represent a game changing technology for the long-term sustainability of the transportation sector. Pursuing this target, a model to simulate an Electric Vehicle (EV) for Formula SAE Electric competition is herein proposed: all the subsystems of the EV and the hybrid storage of the Li-ion batteries and Ultra-Capacitors (UCs) are implemented, in order to store the kinetic energy of the regenerative braking in the storage system through the Kinetic Energy Recovery System (KERS). A bidirectional DC-DC resonant converter is herein applied to the KERS to manage the UC pack. The operational limits of the proposed system, keeping the soft-switching properties, are discussed, and the results show the capability of the converter to operate under resonant mode in both boost and buck mode. A drawback is the presence of high current peaks in the resonant inductor. The use of more than one converter in interleaving and the adoption of a suitable capability factor ensure the proper operation of the system.

Keywords: resonant converter; ultracaps; regenerative braking; electric vehicle

1. Introduction

Today, the awareness of environmental and climatic problems is growing in social and political life. The challenge is to push the technological boundaries to face the sustainability, affordability, and reliability problems of development [1]. Every human activity pays a cost in terms of environmental impact: the whole transportation sector accounts for 20.44% of the global CO_2 emissions according to The World Bank [2] and to the IEA (International Energy Agency) [3]. The rise of global interest in this electric challenge is pushing the traditional automotive industry to develop the required technology. It is in this scenario that in 2013, from the well-known Society of Automotive Engineers, SAE International®, the Formula SAE Electric was born [4]. Hybrid energy storage, such as the combination of Li-ion batteries and Ultra-Capacitor (UC) banks, allows combining devices suitable for storing large amounts of energy with devices suitable for providing power bursts [5]. This energy storage configuration is the best solution for an EV designed to compete in car races in which recurring high power bursts for short times occur during acceleration and regenerative braking [6,7].

The Kinetic Energy Recovery System (KERS) is the set of devices that allows recovering kinetic energy during braking and releasing the recovered energy under acceleration [8]. A power converter is necessary to process and control the flow of electric energy between energy storage and the propulsion system. Resonant converters have several advantageous technical features that make them particularly suited for KERS applications onboard electric racing cars: high power density, low electromagnetic interference (EMI) emissions, high

efficiency, and low commutation losses thanks to soft switching techniques, resulting in compact, lightweight, reliable, and high efficiency converters [9].

The resonant converter topologies are numerous [10]. They can be classified according to topology as Series Resonant Converters (SRCs), Parallel Resonant Converters (PRCs), or series-parallel configurations, depending on the position of the load with respect to the resonant tank, and they may have two or three resonant elements. They may operate in Discontinuous Conduction Mode (DCM) or Continuous Conduction Mode (CCM), and below resonance and above resonance operation are possible. In DCM operation, resonant converters deliver power to the load as a sequence of current pulses with a variable repetition rate. In DC-DC resonant converters, the voltage and current regulation is obtained by a frequency modulation, instead of the duty ratio modulation that characterizes the traditional hard switching Pulse Width Modulation (PWM) converters. Switching frequency control, combined with the nonlinear relation among switching frequency, voltage gain, and load current, increases the control complexity as compared with DC-DC PWM converters operating in CCM, in which the duty ratio regulates the voltage gain regardless of the load current.

This paper proposes a new bidirectional buck-boost resonant converter suitable for KERS applications. Its resonant tank is made of two elements, L and C. DCM operation below resonance frequency is selected as it allows zero current switching (ZCS). The methodological approach chosen for the detailed analysis of the converter was presented in [11]. The converter operation as a buck and boost configuration is analyzed in different time stages by solving the circuit equations in each time interval. The topological states and the operating limits of the resonant converter technology (high efficiency converters [12,13]) to make use of the advantages presented by the UCs are investigated. Besides, the model of the whole EV representing the mechanical, electrical, traction, braking, and storage systems is developed [14], and the resonant converter is included to interface with the UC energy storage of the KERS. The design of the resonant converter, namely the sizing criteria for the resonant tank and the power semiconductor devices, compliant with the EV drivetrain, batteries, and UC pack constraints, is then presented. A detailed analysis is presented and validated through numerical simulations. An interleaved solution and the capability factor are proposed as methods to enhance the KERS converter performance, ensuring the proper operability of the system.

The paper is organized as follows. Section 2 presents the model of the Formula SAE Electric single-seater electric racing car, divided into sub-models connected together. In Section 3, the KERS converter is proposed and its model is derived. Section 4 deals with the KERS resonant converter design and simulation. In the end, some conclusions are stated.

2. Formula SAE Electric Single-Seater Electric Racing Car Model

The main target of the electric racing car model is to compute, at any time step (Δt) of the simulation, all the electric quantities (power, voltage, and current) at the KERS terminals.

Figure 1a shows the block diagram of the complete EV model, where one block for each sub-system of the vehicle is considered, as described in the following. Figure 1b shows the electrical diagram [12] of the EV, where the main elements and the corresponding voltages and currents are represented.

From a given speed profile, the *Pilot* block generates the acceleration and deceleration signals that control the motor and the braking systems, respectively. The *Mechanical Drivetrain* block calculates the net torque applied to the vehicle, which is the input of the *Dynamics* block, where the equations of motion are implemented and the driving variables such as acceleration (a), speed (v), and position (x) are computed. When braking is needed to slow down the EV, the *Braking System* block calculates the available regenerative energy. The model is implemented using power equations to relate the subsystems and regulate the driving simulation [5]. In the following, a detailed description of each block is provided.
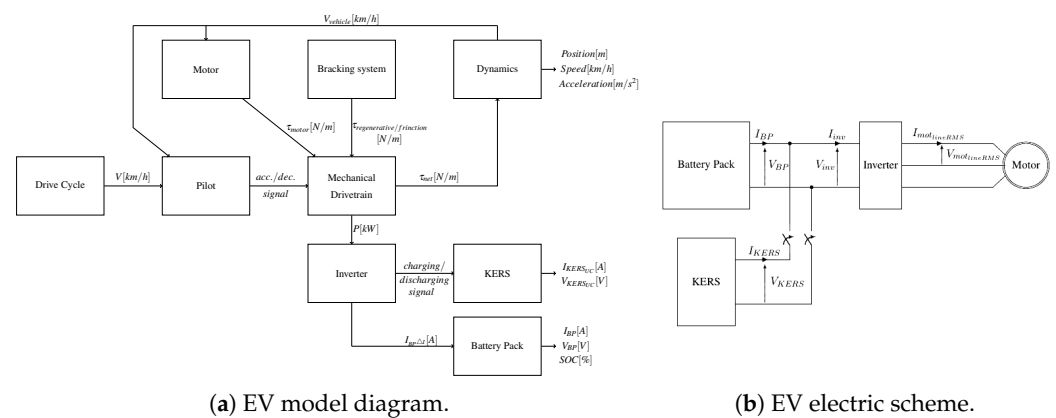
(**a**) EV model diagram.

(**b**) EV electric scheme.

Figure 1. Overall EV model diagram and EV electric scheme. KERS, Kinetic Energy Recovery System.

Drive Cycle block

The *Drive Cycle* block is the source of the reference motion data. Its outputs may be the displacement, the speed, or the acceleration. In this work, as well as in many automotive applications, the reference speed profile is considered, as shown in Figure 2.
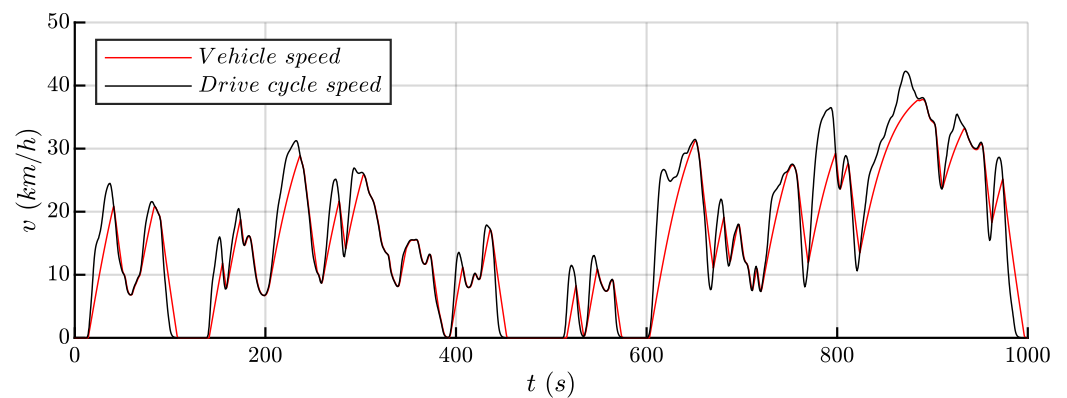

Figure 2. Vehicle speed profile vs. drive cycle speed.

Pilot block

The *Pilot* block receives as input the target speed, from the *Drive Cycle* block, and the actual vehicle speed, from the *Mechanical Drivetrain* block. A PID controller compares these speeds and generates an acceleration or braking signal. Figure 3 shows the action generated by the *Pilot* block.
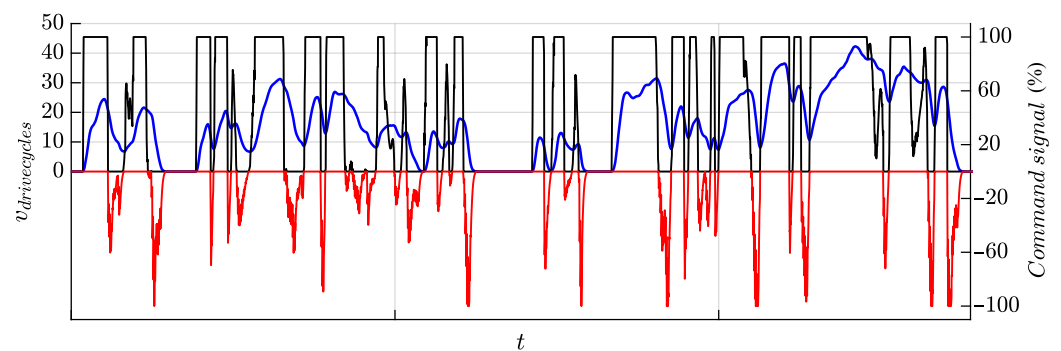

Figure 3. Input speed profile (blue), command signal (black), and acceleration/deceleration signal intensity.

Motor **block**

Starting from the vehicle speed, the *Motor* block provides the torque τ_{mot} generated by the motor according to its torque–speed curve.

Braking **block**

Starting from the braking signal, the *Braking* block compares it with the maximum regenerative torque ($\tau_{reg_{max}}$) and splits the braking torque into the allowed regenerative braking torque (τ_{reg}) and the additional friction braking torque ($\tau_{friction}$) that is required to properly slow down the vehicle.

Mechanical drivetrain **block** Starting from the control signals and the torques generated for the direct (motor traction) or reverse operations (braking), the *Mechanical Drivetrain* passes to the *Dynamics* block the torque (τ_{net}) applied to the vehicle: this is calculated as the algebraic sum of motor torque (τ_{mot}), the braking torque due to friction ($\tau_{friction}$), and the braking torque due to regenerative braking ($\tau_{regenerative}$):

$$\tau_{net} = \tau_{mot} - \tau_{friction} - \tau_{regenerative} \tag{1}$$

During direct operations, the motor torque is greater than zero, while the braking torque due to friction and regenerative braking are both zero. On the contrary, during braking operations, the motor torque is zero and the braking torques due to friction and regenerative braking are non-negative, their values depending on the share between friction and regenerative braking. Figure 4 shows the different components of the torque at the vehicle shaft for motor traction and braking operations.
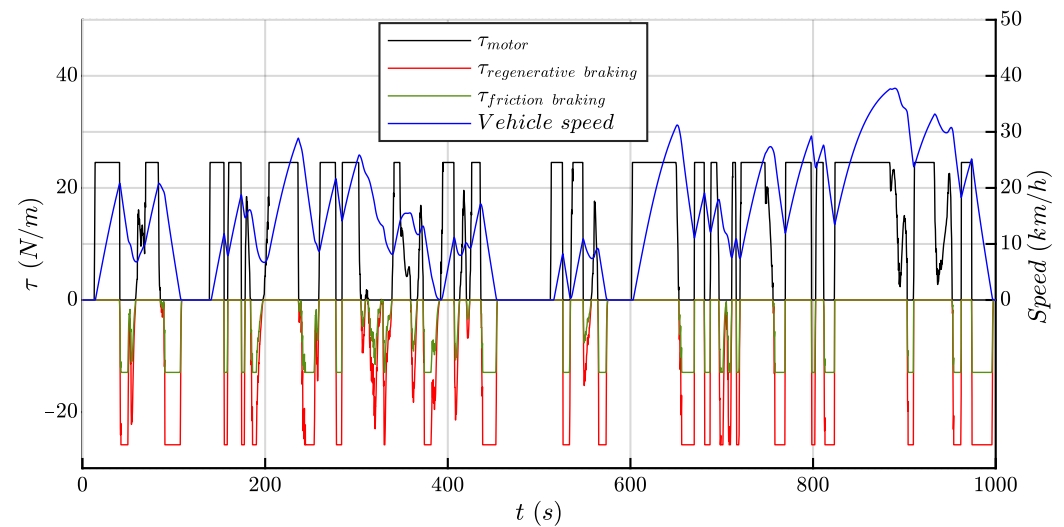

Figure 4. Net torque components.

Dynamics **block**

The *Dynamics* block models the vehicle dynamics by means of the power balance equation. The angular acceleration ($\dot{\omega}_m$), the angular speed (ω_m), as well as the linear acceleration (a), the linear speed (v), and the position (x) are computed in each time step [5]. This analysis is theoretically based and implemented in 2D. The power balance of the EV is:

$$P_{motor} + P_{resistant} + P_{losses} = 0 \tag{2}$$

where the three contributions are defined as follows.

P_{motor} is given by the electromagnetic power generated by the motor minus the power due to the motor inertia:

$$P_{motor} = \tau_m \cdot \omega_m - J_m \cdot \dot{\omega}_m \cdot \omega_m \tag{3}$$

where τ_m is the electromagnetic torque generated by the motor, ω_m is the motor angular speed, $\dot{\omega}_m$ is the motor angular acceleration, and J_m is the motor moment of inertia.

$P_{resistant}$ is the power related to the motion resistances, which are the gravity force on a graded road, friction, aerodynamic force, and inertia:

$$P_{resistant} = -M \cdot g \cdot \sin(\alpha) \cdot v - \tau_{res} \cdot \omega_w - \frac{1}{2} \cdot \rho_{air} \cdot S_{frontal} \cdot C_D \cdot v^3 - J_r^* \dot{\omega}_m \cdot \omega_m \quad (4)$$

where M is the overall weight of both the vehicle and pilot, g is the gravity acceleration, α is the road tilt angle, τ_{res} is the friction torque, ρ_{air} is the density of the air, $S_{frontal}$ is the frontal surface of the vehicle, C_D is the aerodynamic drag coefficient, v is the vehicle speed, and J_r^* is the equivalent vehicle rotational inertia, including the vehicle's and wheels' moment of inertia.

P_{losses} represents the overall losses, assuming them linear with the electromechanical power:

$$P_{losses} = -(1 - \eta) \cdot \tau_m \cdot \omega_m \quad (5)$$

where the efficiency (η) takes into account the overall mechanical losses.

Concerning the inertial terms, they can be easily obtained as the first order derivative of the kinetics energy. For the motor side, it is:

$$\frac{dE_{k_{motor}}}{dt} = \frac{d}{dt}\left(\frac{1}{2} \cdot J_m \cdot \omega_m^2\right) = J_m \cdot \dot{\omega}_m \cdot \omega_m \quad (6)$$

For the vehicle side, the kinetic energy terms due to both vehicle speed and wheels angular speed have to be taken into account:

$$\frac{dE_{k_{vehicle}}}{dt} = \frac{d}{dt}\left(4 \cdot \left(\frac{1}{2} \cdot J_w \cdot \omega_w^2\right) + \frac{1}{2} \cdot M \cdot v^2\right) = J_r^* \cdot K_{tr}^2 \cdot \dot{\omega}_m \cdot \omega_m \quad (7)$$

where ω_w is the wheels' angular speed, J_w is the wheels' moment of inertia, R_w is the wheel radius, and K_{tr} is the transmission ratio; as a consequence, $v = \omega_w \cdot R_w = K_{tr} \cdot \omega_m \cdot R_w$. In this work, K_{tr} is introduced for the sake of completeness; for an EV, it is usually equal to one.

The resistant torque τ_{res} in (4) can be better represented by substituting the following relations:

$$\tau_{res} = M \cdot g \cdot \cos(\alpha) \cdot f_d \cdot R_w \quad (8)$$

where $M \cdot g \cdot \cos(\alpha)$ is the net ground reaction force and f_d is the dynamic friction.

By substituting (8) in (4) and substituting (3–5) in (2), the equation of motion becomes:

$$\eta \cdot (\tau_m - J_m \cdot \dot{\omega}_m) \cdot \omega_m = M \cdot g \cdot [f_d \cdot \cos(\alpha) + sen(\alpha)] \cdot R_w \cdot K_{tr} \cdot \omega_m +$$
$$+ \frac{1}{2} \cdot \rho_{air} \cdot S_{frontal} \cdot C_D \cdot \omega_m^3 \cdot R_w^3 \cdot K_{tr}^3 + J_r^* \cdot \dot{\omega}_m \cdot \omega_m \cdot K_{tr}^2 \quad (9)$$

Here, the net power at the motor side minus the motor inertia is equal to the sum of the rolling and grading resistances, the aerodynamic drag, and the vehicle inertia.

The angular acceleration, as well as the linear speed and the position are derived from the solution of (9).

***Inverter and Storage Management* block**

Starting from the absolute value of the electromechanical power required for motion, the *Inverter and Storage Management* block calculates the absolute value of the power and current at the inverter DC side (P_{inv}), as follows:

$$P_{inv} = \begin{cases} \eta_{md} \cdot P_{motor} & \text{braking operation} \\ \frac{P_{motor}}{\eta_{md}} & \text{motor traction} \end{cases} \qquad I_{inv_{DC}} = \frac{P_{inv}}{V_{inv}} \quad (10)$$

where η_{md} is the overall efficiency of the motor drive, P_{motor} is the absolute value of the electromechanical power generated by the motor, and V_{inv} is the voltage of the vehicle DC bus, which is the same voltage applied both to the battery pack terminals (V_{BP}) and to the

DC bus side KERS converter terminals (V_{KERS}). Depending on direct or reverse operation, a control signal is generated to control the KERS and to split the inverter current into the battery pack current (I_{BP}) and the KERS current (I_{KERS}).

Battery Pack block

Starting from the battery pack (BP) current (I_{BP}) as input, *Battery Pack* block calculates the State of Charge (*SOC*) and the corresponding voltage (V_{BP}) per each time step (Δt). The minimum levels of *SOC* and V_{BP} work as a backstop function, and they set the operational limit to guarantee the reliability and durability of the batteries.

The battery pack model is based on the Butler–Volmer physical approach [15]. The equation that describes how the electrical current (*i*) through an electrode depends on the voltage difference between the electrode and the bulk electrolyte is:

$$i = n_s F \left(k_o a_o^{v_o} e^{\frac{\beta_o F(E+\eta)}{RT}} - k_r a_r^{v_r} e^{\frac{-\beta_r F(E+\eta)}{RT}} \right) \tag{11}$$

where the subscripts *o* and *r* indicate the state for oxidation and reaction, respectively, n_s is the number of the electrochemical steps excluding repetitions, k_o and k_r are the chemical equilibrium coefficients, $a_o^{v_o}$ and $a_r^{v_r}$ are the activity coefficients, *F* is the Faraday constant, η is the overpotential, and *E* is the equilibrium electrode potential. The overall cell voltage V_{cell} is:

$$V_{cell} = E^+ + \eta^+ - E^- - \eta^- - \eta_{el} \tag{12}$$

The BP works as the main storage source of the vehicle. The battery pack layout is derived from the voltage (V_{inv}) and from the current (I_{inv}) requirements at the inverter DC side.

The number of cells in series (n_s) and the number of strings in parallel (n_p) are defined as:

$$n_s = \frac{V_{inv}}{V_{cell}} \quad ; \quad n_p = \frac{I_{inv}}{I_{cell_{NOM}}} \tag{13}$$

where V_{cell} is the rated no-load voltage of each cell and $I_{NOM_{cell}}$ is the rated cell current. Figure 5 shows the input of the *Battery Pack* block, that is the current at the BP terminals (I_{BP}), and the outputs, which are the voltage at the BP terminals (V_{BP}) and its State of Charge (*SOC*), along the whole drive cycle.

KERS block

The *KERS* block receives as input the logic signal from the inverter and storage management block, which is a request to activate, and calculates the KERS current (I_{KERS}), which depends on the state of charge of the UC pack (SOC_{UC}) and the allowable charge and discharge current (I_{UC}). Figure 6 shows the input of the *KERS* block, which is the regulation signal, and the outputs, which are the current (I_{KERS}) and the voltage ($V_{UC_{pack}}$) at the UC terminals, along the whole drive cycle. The UC pack is sized as the BP.

The aim of this additional system is to exploit the UC peculiarities of high current capability, thermal stability, long ELD (Estimated Life Duration), and very fast behavior in both charge and discharge, to help the BP in the most critical driving phases. As shown in the first graph in Figure 6, the current capability decreases proportionally to the voltage drop during discharge. In the second graph, the voltage behavior of the UC pack is represented. The discharge voltage is limited by $V_{UCpack_{MIN}}$. When the voltage of the UC pack reaches the minimum value, the KERS stops operating. In the last graph, the signal that controls the regeneration during braking is displayed, where 1 means ON, while 0 is OFF.
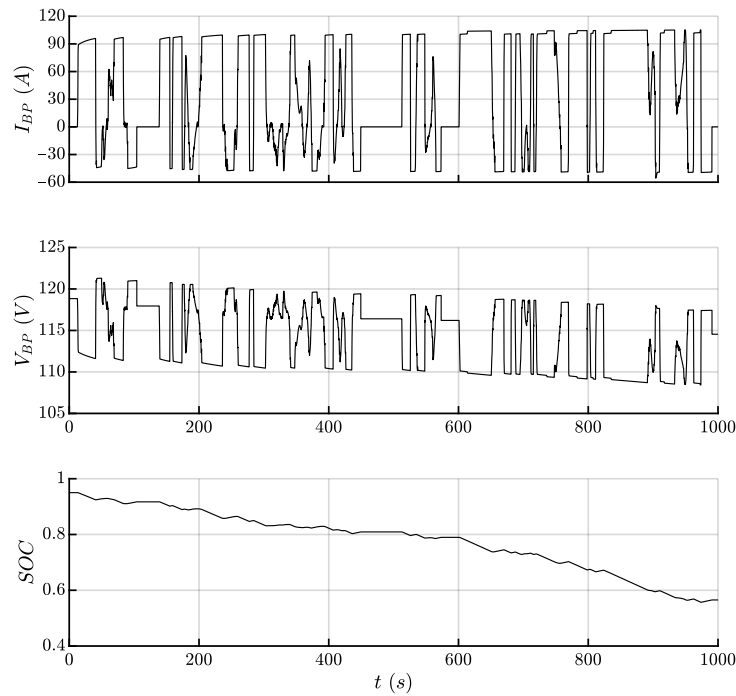
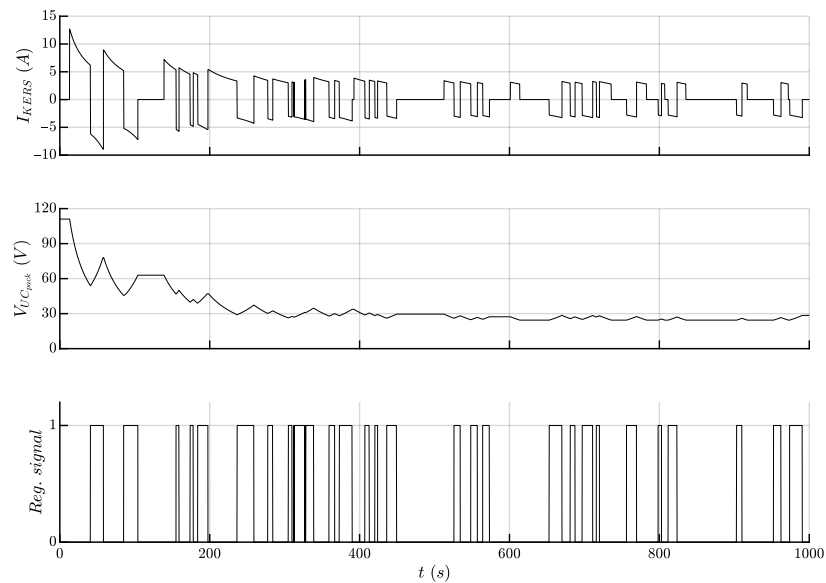**Figure 5.** Battery pack current, battery pack voltage, and state of charge.

Figure 6. KERS current, resulting UC voltage, and regeneration brake control signal (Reg. signal).

3. KERS Converter

Resonant converters are suitable for KERS applications [12,13] due to their features of high efficiency at high switching frequency, their compactness, and their scalability. The small size of the passive components and high power density can be achieved by increasing the switching frequency. In contrast to conventional PWM converters that are based on hard switching and suffer from high switching losses [16], resonant converters use a resonant tank—an $L - C$ circuit—to turn on and turn off at zero current (ZCS) or zero voltage (ZVS) [17], resulting in negligible switching losses [18], hence high efficiency and small heat sinks [19]. The converter proposed in this work is a bidirectional ZCS converter presented by Figure 7. The bidirectional capability is obtained by adding switches S_1 and

S_2 and diodes D_3 and D_4 to the original boost converter presented in [13]. This improved topology can also operate as a buck converter transferring energy from V_{out} to V_{in}.
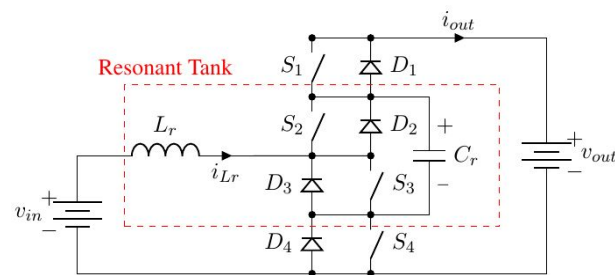

Figure 7. Resonant buck-boost converter.

3.1. Topology Analysis

The operation principle, both in boost mode and in buck mode, as well as the characteristics of the chosen converter for the EV application as the KERS interface are presented here. The converter analysis is based on the following assumptions [20,21]:

- the converter is analyzed in the steady state;
- the switches and the diodes are treated as being ideal;
- losses in the inductive and capacitive elements of the resonant tank are neglected;
- the voltages at the input and output terminals are assumed to be constant.

3.1.1. Boost Analysis

In boost operation mode, the pair of switches S_3 and S_4 is controlled by a complementary square-wave with a 50% duty cycle D_i, and the pair of switches S_1 and S_2 is kept in the off state. Each half switching cycle consists of three stages, as illustrated in Figure 8.

(**a**) Stage 1 (boost).

(**b**) Stage 2 (boost).

(**c**) Stage 3 (boost).
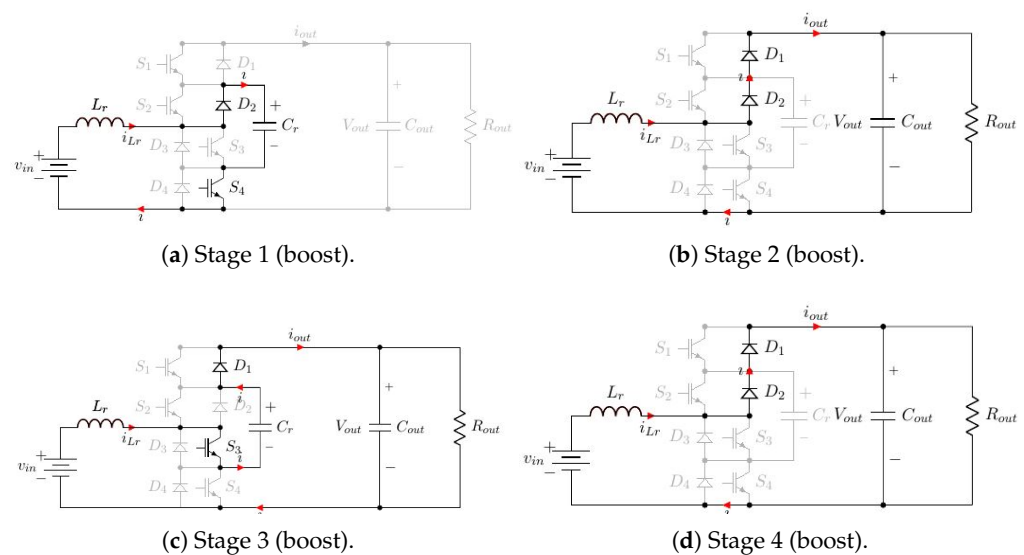
(**d**) Stage 4 (boost).

Figure 8. Representation of the topological stages.

Stage 1 $[t_0, t_1]$

At the beginning of the switching period at t_0:

- the resonant tank capacitor C_r and the resonant tank inductor L_r are uncharged;
- S_3 turns off, and S_4 turns on;
- D_2 results in forward bias, and D_1 results in reverse bias.

When S_4 turns on, the resonant tank charges C_r through the inductor L_r. At t_1, the voltage across C_r reaches the output voltage level V_{out}, D_1 becomes forward biased, and this transient ends. The inductor current is $I_{1,boost}$. The state-space equations of this stage are:

$$\begin{cases} V_{in} = L_r \frac{di_{Lr}}{dt} + v_{Cr}(t) \\ i_{Lr}(t) = C_r \frac{dv_{Cr}(t)}{dt} \end{cases} \tag{14}$$

The solution of (14) in the Laplace domain [10] is:

$$\begin{cases} I_{Lr}(s) = \frac{C_r}{s^2 L_r C_r + 1} V_{in} \\ V_{Cr}(s) = \frac{V_{in}/s}{1 + s^2 L_r C_r} \end{cases} \tag{15}$$

The inverse Laplace transformation [10] gives:

$$\begin{cases} i_{Lr}(t) = \frac{\sin(\omega_0 t)}{\omega_0} \frac{V_{in}}{L_r} \\ v_{Cr}(t) = V_{in}[1 - \cos(\omega_0 t)] \end{cases} \tag{16}$$

where $\omega_0 = \frac{1}{\sqrt{L_r C_r}}$ is the resonant angular frequency.

In order to get generic results, the per unit state variables, $\overline{i_{Lr}(t)}$ and $\overline{v_{Cr}(t)}$, are introduced:

$$\begin{cases} \overline{i_{Lr}(t)} = \frac{i_{Lr}(t)}{V_{in}/Z_r} \\ \overline{v_{Cr}(t)} = \frac{v_{Cr}(t)}{V_{in}} \end{cases} \tag{17}$$

where $Z_r = \sqrt{\frac{L_r}{C_r}}$ is the resonant impedance. Finally, the per unit state variables are included in the state vector z:

$$z = \overline{v_{Cr}(t)} + j\overline{i_{Lr}(t)} \tag{18}$$

Stage 1 is described by the following state vector:

$$z_{1,boost} = (1 - \cos(\omega_0 t)) + j(\sin(\omega_0 t)) \tag{19}$$

Assuming the boost mode voltage gain defined as $G_{boost} = \frac{V_{out}}{V_{in}}$, the capacitor voltage at the end of Stage 1 is G_{boost}. Therefore, the duration of the first stage is:

$$\Delta t_{10} = t_1 - t_0 = \frac{1}{\omega_0}(\pi - \arccos(G_{boost} - 1)) \tag{20}$$

The resulting per unit inductor current is:

$$\overline{i_{Lr}(t_1)} = \overline{I_{1,boost}} = \frac{I_{1,boost}}{V_{in}/Z_r} = \sin(\omega_0 \Delta t_{10}) \tag{21}$$

Stage 2 $[t_1, t_2]$

At the beginning of Stage 2 at t_1:

- $v_{Cr}(t_1)$ is equal to V_{out}, and $i_{Lr}(t_1)$ is equal to $I_{1,boost}$;
- S_3 is still off, and S_4 is still on;
- D_2 is still forward biased, and D_1 results in forward bias.

$v_{Cr}(t)$ is equal to V_{out}, and $i_{Lr}(t)$ drops linearly to zero. As soon as the current in the inductor reaches zero, diode D_2 becomes reverse biased ($V_{out} > V_{in}$) and Stage 2 ends. The state vector during Stage 2 is:

$$z_{2,boost} = (G_{boost}) + j(\omega_0(1 - G_{boost}) + \overline{I_{1,boost}}) \tag{22}$$

The duration of this stage can be calculated as:

$$\Delta t_{21} = t_2 - t_1 = \frac{1}{\omega_0} \frac{\overline{I_{1,boost}}}{G_{boost} - 1}$$

(23)

Stage 3 $[t_2, t_3]$

　　At the beginning of Stage 3 at t_2:

- $i_{Lr}(t)$ has just reached zero, and $v_{Cr}(t)$ is clamped at V_{out};
- S_3 is still off, and S_4 is still on;
- D_2 results in reverse bias, and D_1 is still forward biased.

　　$i_{Lr}(t) = 0$, and there is no power transfer at the converter input terminals. The state vector during Stage 3 is $z_{3,boost} = G_{boost}$. It ends at half of the whole switching cycle: $\omega_s t = \pi$. Therefore:

$$\omega_s \Delta t_{32} = \pi - \omega_s \Delta t_{21} - \omega_s \Delta t_{10}$$

(24)

Stage 4 $[t_3, t_4]$

　　At the beginning of Stage 4 at t_3, that is the beginning of the second half of the switching period:

- $v_{Cr}(t_1)$ is equal to V_{out}, and $i_{Lr}(t_1)$ is equal to zero;
- S_3 turns on, and S_4 turns off;
- D_1 results in forward bias, and D_2 results in reverse bias.

　　Stage 4 is similar to Stage 1. The turning on of S_3 triggers the transient of the resonant tank that discharges C_r. At t_4, v_{Cr} drops to zero, D_2 becomes forward biased, and the transient ends. The Laplace transform of the state space equations during Stage 4 is:

$$\begin{cases} I_{Lr}(s) = \frac{C_r}{s^2 L_r C_r + 1} V_{in} \\ V_{Cr}(s) = \frac{V_{out}}{s} - \frac{V_{in}/s}{1 + s^2 L_r C_r} \end{cases}$$

(25)

　　The state vector during Stage 4 is:

$$z_{4,boost} = (G_{boost} - 1 + \cos(\omega_0 t)) - j(\sin(\omega_0 t))$$

(26)

　　The duration of Stage 4 is the same as Stage 1 ($\Delta t_{43} = \Delta t_{10}$), and the inductor current at the end of Stage 4 is $I_{4,boost} = I_{1,boost}$.

Stage 5 $[t_4, t_5]$

　　At the beginning of Stage 5 at t_4:

- $v_{Cr}(t_1)$ is equal to zero, and $i_{Lr}(t_1)$ is equal to $I_{4,boost}$;
- S_4 is still off, and S_3 is still on;
- D_2 is still forward biased, and D_1 results in forward bias.

　　Stage 5 is similar to Stage 2. The current I_{Lr} reduce linearly to zero; the initial current is the same as Stage 2, as well as the voltage applied to L_r. The state vector during Stage 5 is:

$$z_{5,boost} = 0 + j(\omega_0(1 - G_{boost}) + \overline{I_{1,boost}})$$

(27)

　　The duration of Stage 5 is the same as Stage 2 ($\Delta t_{54} = \Delta t_{21}$).

Stage 6 $[t_5, t_6]$

　　At the beginning of Stage 6 at t_5:

- $i_{Lr}(t)$ has just reached zero, and $v_{Cr}(t)$ is zero;
- S_4 is still off, and S_3 is still on;
- D_1 results in reverse bias.

Stage 6 is similar to Stage 3. There is no power transfer at the converter input terminals. The state vector is $z_{6,boost} = 0$. The duration of Stage 6 is the same as Stage 3 ($\Delta t_{65} = \Delta t_{32}$), and the end of Stage 6 corresponds to the end of the switching cycle.

3.1.2. Buck Analysis

In buck operation mode, the pair of switches S_1 and S_2 is controlled by a complementary square-wave with a 50% duty cycle D_i, and the pair of switches S_3 and S_4 is kept in the off state. Like in boost operation mode, each half switching cycle consists of three stages, as illustrated in Figure 9. Each stage is similar to the corresponding stage in boost operation mode, and it is modeled in the same way.
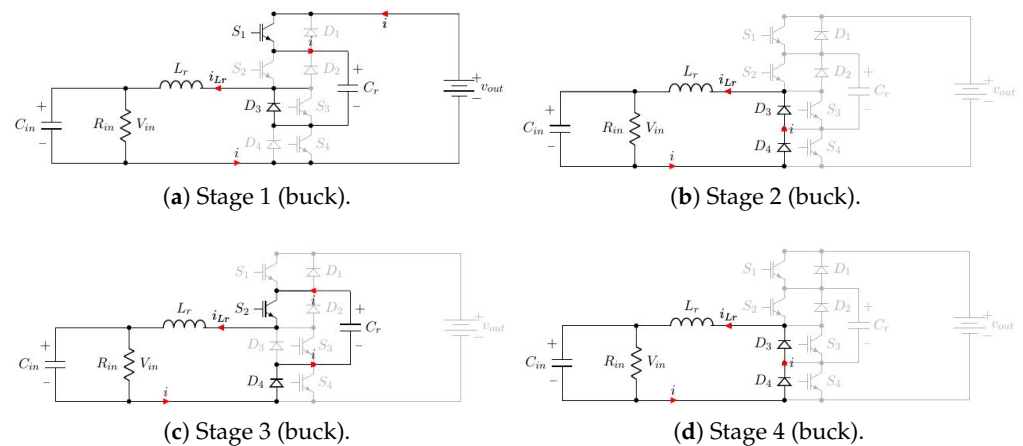

(**a**) Stage 1 (buck).   (**b**) Stage 2 (buck).

(**c**) Stage 3 (buck).   (**d**) Stage 4 (buck).

Figure 9. Representation of the buck topological stages.

Stage 1 $[t_0, t_1]$

At the beginning of the switching period, t_0:

- $v_{Cr}(t_1)$ is equal to zero, and $i_{Lr}(t_1)$ is equal to zero;
- S_2 turns off, and S_1 turns on;
- D_3 results in forward bias, and D_4 results in reverse bias.

The turning on of S_1 triggers the transient of the resonant tank that charges C_r, which ends at t_1, when $v_{Cr}(t_1) = V_{out}$, and D_4 becomes forward biased. The state vector and the duration of Stage 1 are:

$$\begin{cases} z_{1,buck} = ((\frac{1}{G_{buck}} - 1)(1 - \cos(\omega_0 t))) + j((\frac{1}{G_{buck}} - 1)\sin(\omega_0 t)) \\ t_{10} = t_1 - t_0 = \frac{1}{\omega_0}(\pi - \arccos(\frac{G_{buck}}{G_{buck}-1})) \end{cases} \quad (28)$$

where $G_{buck} = \frac{V_{in}}{V_{out}}$. The inductor current at the end of Stage 1 is:

$$I_{1,buck} = (G_{buck} - 1)\sin(\omega_0 \Delta t_{10}) \quad (29)$$

Stage 2 $[t_1, t_2]$

At the beginning of Stage 2, t_1:

- $v_{Cr}(t_1)$ is equal to V_{out}, and $i_{Lr}(t_1)$ is equal to $I_{1,buck}$;
- S_2 is still off, and S_1 is still on;
- D_3 is still forward biased, and D_4 results in forward bias.

During Stage 2, $v_{Cr}(t)$ is clamped at V_{out} and $i_{Lr}(t)$ drops linearly to zero. As soon as the current in the inductor reaches zero, diode D_3 becomes reverse biased ($V_{out} > V_{in}$) and Stage 2 ends. The state vector and the duration of Stage 2 are:

$$\begin{cases} z_{2,buck} = \left(\frac{1}{G_{buck}}\right) + j(\overline{I_{1,buck}} - \omega_0(t - t_1)) \\ \Delta t_{21} = t_2 - t_1 = \frac{\overline{I_{1,buck}}}{\omega_0} \end{cases} \tag{30}$$

Stage 3 $[t_2, t_3]$

At the beginning of Stage 3, t_2:

- $i_{Lr}(t)$ has just reached zero, and $v_{Cr}(t)$ is clamped at V_{out};
- S_3 is still off, and S_4 is still on;
- D_3 results in reverse bias, and D_4 is still forward biased.

The state vector during Stage 3 is $z_{3,buck} = \frac{1}{G_{buck}}$. Stage 3 ends at half of the whole switching cycle, which means $\omega_s t = \pi$. Therefore:

$$\omega_s \Delta t_{32} = \pi - \omega_s \Delta t_{21} - \omega_s \Delta t_{10} \tag{31}$$

Stage 4 $[t_3, t_4]$

At the beginning of Stage 4, t_3:

- $v_{Cr}(t_1)$ is equal to V_{out}, and $i_{Lr}(t_1)$ is equal to zero;
- S_2 turns on, and S_1 turns off;
- D_4 results in forward bias, and D_3 results in reverse bias.

Like Stage 1, the turning on of S_3 triggers the transient of the resonant tank that discharges C_r. As soon as v_{Cr} has dropped to zero, at t_4, D_3 becomes forward biased and this transient ends. The resulting state vector during Stage 4 is:

$$z_{4,buck} = \left(\frac{1}{G_{buck}} - 1 + \cos(\omega_0 t)\right) - j\left(\frac{1}{G_{buck}} \sin(\omega_0 t)\right) \tag{32}$$

As a result, the duration of Stage 4 is the same as Stage 1 ($\Delta t_{43} = \Delta t_{10}$) and the inductor current at the end of Stage 4 is $I_{4,buck} = I_{1,buck}$.

Stage 5 $[t_4, t_5]$

At the beginning of Stage 5, t_4:

- $v_{Cr}(t_1)$ is equal to zero, and $i_{Lr}(t_1)$ is equal to $I_{4,buck}$;
- S_1 is still off, and S_2 is still on;
- D_4 is still forward biased, and D_3 results in forward bias.

Stage 5 is similar to Stage 2: the current I_{Lr} reduces linearly to zero, then D_4 becomes reverse biased. The state vector of Stage 5 is:

$$z_{5,buck} = 0 + j(\overline{I_{1,boost}} - \omega_0(t - t_4)) \tag{33}$$

The duration of Stage 5 is the same as Stage 2 ($\Delta t_{54} = \Delta t_{21}$).

Stage 6 $[t_5, t_6]$

During all of Stage 6:

- $i_{Lr}(t)$ is equal to zero, and $v_{Cr}(t)$ is equal to zero;
- S_1 is still off, and S_2 is still on;
- D_4 results in reverse bias.

The state vector during Stage 6 is $z_{6,buck} = 0$, and the duration of Stage 6 is the same as Stage 3 ($\Delta t_{65} = \Delta t_{32}$). The end of Stage 6 corresponds to the end of the switching cycle.

3.2. Resonant Converter Characteristics

In this section, starting from the six different stages' analysis, the characteristics in terms of voltage gain as a function of the control strategies and the load are calculated.

In order to keep the soft switching properties, the boost gain is limited to the range $1 < G_{boost} < 2$ and the switching frequency should not exceed the resonant frequency. The stable operation during Stage 2 sets the lower boundary for V_{out}. The maximum voltage across the resonant capacitor at the end of Stage 1 ($2V_{in}$) sets the upper boundary for V_{out}. The maximum duration of Stage 1 sets the upper boundary for the switching frequency f_s, which has to be lower than or equal to the resonant frequency f_0.

The output current in boost mode is discontinuous and is zero during Stages 1, 3, and 6. The average per unit output current $\overline{i_{outAVG}}$ results in:

$$\overline{i_{outAVG}} = \frac{1}{T_s}[\int_{T_s} \overline{i_{Lr}(t)}dt] = \frac{\mu_0}{2\pi}\frac{G_{boost}}{(G_{boost} - 1)} \tag{34}$$

where $\mu_0 = \frac{f_s}{f_0}$. The output power is consequently:

$$\overline{P_{outAVG}} = \frac{\mu_0}{2\pi}\frac{G_{boost}^2}{(G_{boost} - 1)} \tag{35}$$

Figure 10 shows the output characteristics as a function of frequency ratio μ_0 and boost voltage gain G_{boost}. For a given frequency ratio μ_0, the output power reduces with the increase of the boost voltage gain G_{boost}. For a given voltage gain G_{boost}, the output power increases with the frequency ratio μ_0.
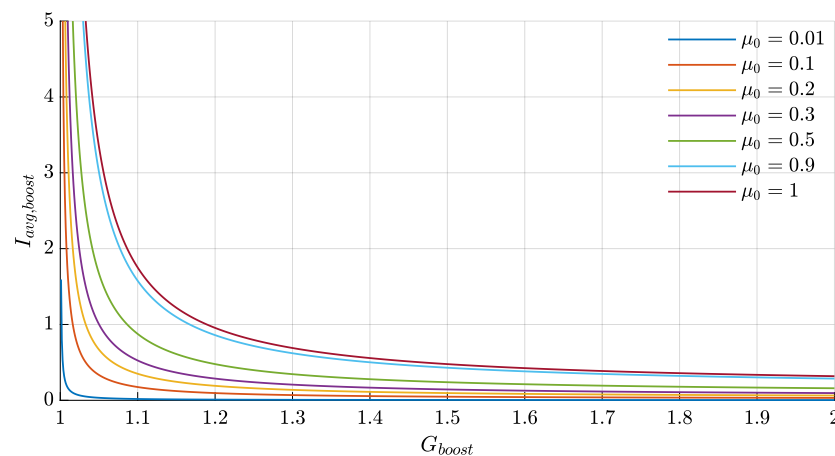

Figure 10. Output current as a function of voltage gain; the switching frequency is a parameter.

The converter operation as a function of the load depends on the output apparent resistance $R_{out} = \frac{V_{out}}{I_{outAVG}}$. In order to get generic results, the per unit output resistance is:

$$r_{out} = \frac{R_{out}}{Z_r} \tag{36}$$

The voltage gain in boost mode, as a function of the frequency ratio and per unit load, is:

$$G_{boost} = \frac{\mu_0}{2\pi}r_{out} + 1 \tag{37}$$

Since $0 < \mu_0 < 1$, the converter can adjust the voltage gain in the whole range ($1 < G_{boost} < 2$) for loads whose per unit apparent resistance is greater than 2π.

For the buck configuration, the average input current i_{inAVG} can be calculated as the sum of the integral of the current function in the topological time steps Δt_{10}, Δt_{21}, Δt_{43}, and Δt_{54}:

$$\overline{i_{inAVG}} = \frac{1}{T_s}[\int_{t_0}^{t_1} \overline{i_{Lr}(t)}dt + \int_{t_1}^{t_2} \overline{i_{Lr}(t)}dt + \int_{t_3}^{t_4} \overline{i_{Lr}(t)}dt + \int_{t_4}^{t_5} \overline{i_{Lr}(t)}dt] \tag{38}$$

Solving:

$$\overline{i_{inAVG}} = \frac{\mu_0}{2\pi} \frac{1}{G_{buck}} \tag{39}$$

The dependency of $\overline{i_{inAVG}}$ on the frequency ratio μ_0 and the gain G_{buck} shows the same trend as the boost one.

The buck gain range is $0 < G_{buck} < 0.5$.

Considering the input voltage V_{in} approximately constant, a constant load resistance R_{in}, the average input current (39), and defining $r_{in} = \frac{R_{in}}{Z_r}$, the gain of the buck modulation is:

$$G_{buck} = \sqrt{r_{in} \frac{\mu_0}{2\pi}} \tag{40}$$

Considering the maximum switching frequency as equal to the resonant one results in: $0 < \mu_0 < 1$. Indeed, to reach the maximum gain $G_{buck} = 0.5$, the minimum value of r_{in} to be considered is 1.571.

4. Resonant Converter Design and Simulation Results

4.1. Design Methodology

The design process of the resonant converter followed these main steps:

1. The definition of the optimal gain range for both boost and buck operations;
2. The identification, through the parameterized analysis, of the optimal value for the parameterized load r_0;
3. Setting the maximum allowable peak current (I_{peak}) in the resonant inductor, switches, and diodes;
4. The choice of the switching technology for the required resonant frequency f_0;
5. Checking the UC pack current capability over both the charge and discharge operations.

As already discussed, in order to keep the soft switching properties, the maximum possible gain for boost operation mode is $1 < G_{boost} < 2$ and for buck operation mode is $0 < G_{buck} < 0.5$.

Therefore, a minimum UC pack voltage has to be set, and this limits the buck resonant operation. Therefore, the optimization process is performed based on boost mode. This means keeping as the objective: $r_{out} > 2\pi$. The resonant frequency f_0 is set based on the choice of the switches' technology. Then, once the nominal voltage for the UC pack $\frac{V_{UCpack}}{G_{boost}}$, where $G_{boost} = 2$, the resonant frequency $f_0 = \frac{1}{2\pi\omega_0}$, the resonant impedance $Z_r = \sqrt{\frac{L_r}{C_r}}$, and the resonant angular frequency μ_0 are defined, the values of the resonant components are set in accordance with the equations below:

$$L_r = \frac{Z_r}{2\pi f_0} \qquad C_r = \frac{1}{2\pi Z_r f_0} \tag{41}$$

The switching frequency for boost operation mode is selected using (34) and (37) as:

$$f_{s_{boost}} = \frac{G-1}{R_{out} C_r} \tag{42}$$

Instead, the switching frequency for buck operation mode is defined using (39) and (40):

$$f_{s_{buck}} = \frac{G_{buck}^2}{R_{UC_{pack}} C_r} \tag{43}$$

where R_{UCpack} is the UC pack apparent resistance.

Keeping under control all the component and project constraints already mentioned, the most stringent requirement for this application is derived:

$$I_{peak_{Lr}} > \frac{2\pi V_{inv}}{R_{out}} \tag{44}$$

Since V_{inv} should be approximately constant during operation and $R_{out} = \frac{V_{inv}^2}{P_{inv}}$ is very low, the minimum possible value for $I_{peak_{Lr}}$ is very high. Moreover, thus results in a peak current at the input terminals of the UC pack.

To reduce the impact of the high peak current on the resonant converter design, two solutions can be adopted:

1. Reduce the power capability of the converter; a capability factor k is defined setting the maximum gain of the converter $G_{boost} = 2$ and the maximum input current at the UC pack $I_{UCpack} = I_{max}$:

$$k = \frac{I_{UCpack} \frac{V_{UCpack}}{G_{boost}}}{P_{inv}} \tag{45}$$

Therefore, the capability of the system P_{KERS} is defined by $P_{KERS} = kP_{inv}$.

2. Use more than one converter in interleaving mode [22,23]; assuming a reasonable number of converters ($n_{res_{conv}} = 2$), the power capability of each one becomes:

$$P_{res_{conv}} = k\frac{P_{inv}}{n_{res_{conv}}} \tag{46}$$

This choice can halve the power capability of each converter, thus the input current, while increasing the current peak to the UC pack of just a factor of $\sqrt{2}$. The resulting peak current in the UC pack is:

$$I_{UCpack_{peak}} = \sqrt{2}I_{peak_{Lr}} \tag{47}$$

Combining these two effects, it is possible to define the whole system capability value k that makes each resonant converter respect all the constraints:

$$k = \frac{I_{UCpack_{max}} V_{inv}^2 n_{res_{conve}}}{2\pi\sqrt{2}V_{UCpack}P_{inv}} \tag{48}$$

Therefore, the converter can exploit the boost resonant characteristics along all the allowable gain range, and the working limits of buck operation in current, gain, and switching frequency are reported in the Figure 11. Table 1 reports the design and simulation data considered in this paper.
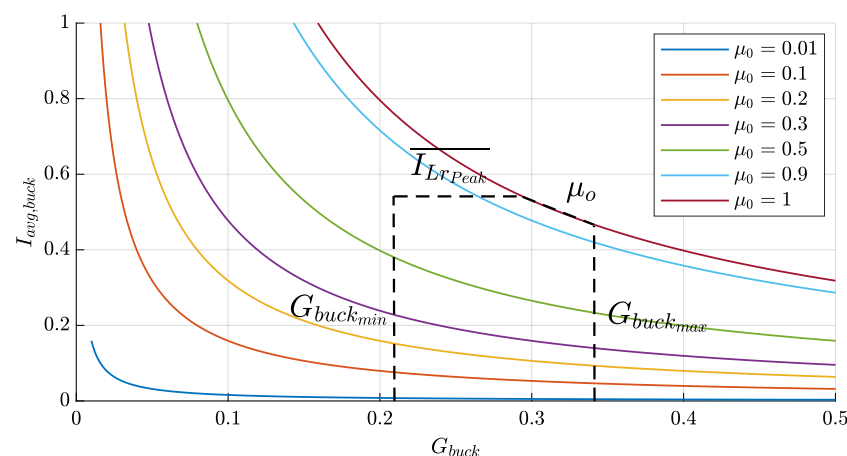

Figure 11. Current, gain, and switching frequency: limits in buck operations.

Table 1. Design and simulation data.

Symbol	Quantity	Value	Units
Z_r	Resonant impedance	0.9694	(Ω)
L_r	Resonant inductor	7.71×10^{-7}	(H)
C_r	Resonant capacitor	8.21×10^{-7}	(F)
ω_0	Resonant angular frequency	0.1256×10^6	(rad/s)
k	System capability	16	(%)
$P_{res.conv}$	Resonant converter power capability	1.0122	(kW)
R_{out}	Equivalent resonant converter output resistance	11.18	(Ω)
r_{in}	Parameterized input resistance	0.733	–
G_{buck}	Buck gain	0.3	–
f_{sbuck}	Buck switching frequency	154.2	(kHz)
f_0	Resonant frequency	200	(kHz)
$R_{snubber}$	Snubber resistance	10×10^5	(Ω)
R_{ons}	Internal resistance	10×10^{-5}	(Ω)
$C_{snubber}$	Snubber capacitance	inf	(F)
G_{boost}	Nominal boost gain	2	–
$n_{res.conv}$	Number of resonant converter	2	–
r_{out}	Parameterized output resistance	2π	–

Outside the boost and buck resonant areas, a change in modulation strategy from resonant to a conventional PWM operation is required (hybrid modulation). However, going through the KERS analysis as designed, it appears clear that the contribution of the system to the whole current required is pretty low. Figure 12 shows that, despite the full charge of the UC pack, the KERS is not able to provide or absorb more than 15% of the total current.
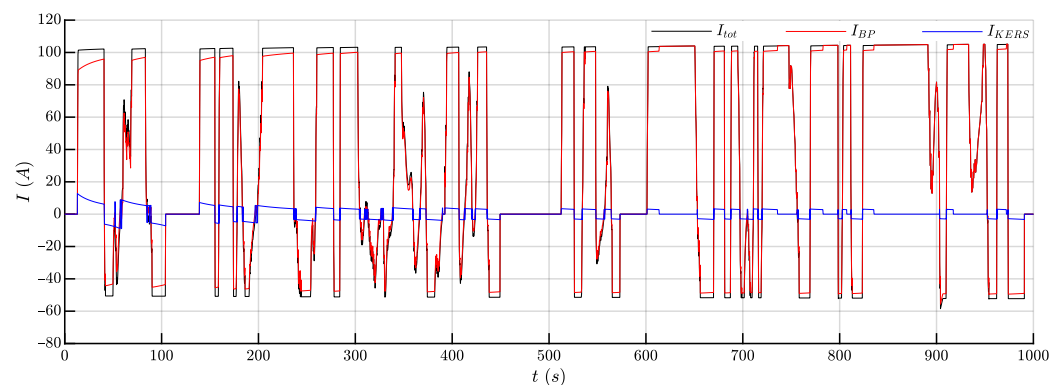
Figure 12. Currents along the whole drive cycle: KERS current (blue), battery pack current (red), and total current (black).

The peak current in the resonant inductor (I_{Lr}) depends on the specific operating conditions. The reason just analyzed in (44) is appreciable from Figure 13: at $G_{boost} = 2$, while I_{Lr} is greater than 70 A, the average output current is around 10 A (for each converter).

Furthermore, to avoid inductor current saturation in any working condition, it shall be designed at a higher value than the peak current. Therefore, considering the DCM behavior of the converter, the main drawback is the low average current capability compared to the weight and dimensions of the resonant inductor. Then, since during the race (as well as in the simulated speed cycle shown in Figure 2), the acceleration times are much longer and more frequent than the braking ones and since the KERS system is not able to absorb an important amount of the braking energy, the UC pack quickly runs out of charge.
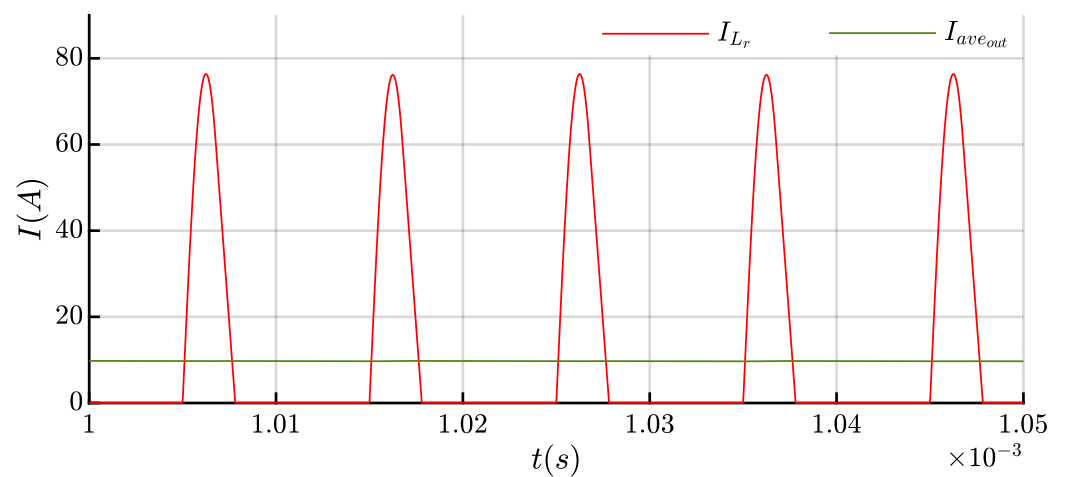
Figure 13. Inductor peak current and average output current.

4.2. Resonant Converter Simulation Results

For boost switching mode, the main waveforms of the voltages and currents of the components are shown in Figure 14. As expected from theory, the resonant capacitor V_{Cr} is charged to V_{out} and then clamped at this value during the first half switching cycle. Then, in the second half switching cycle, the resonant capacitor is discharged to zero. The frequency of the current through the resonant inductor i_{Lr} is twice the switching frequency. The average value of the current through the diodes is dependent on the switching frequency, then the output voltage can be regulated by varying the ratio between the switching frequency and the resonant frequency (μ_0).
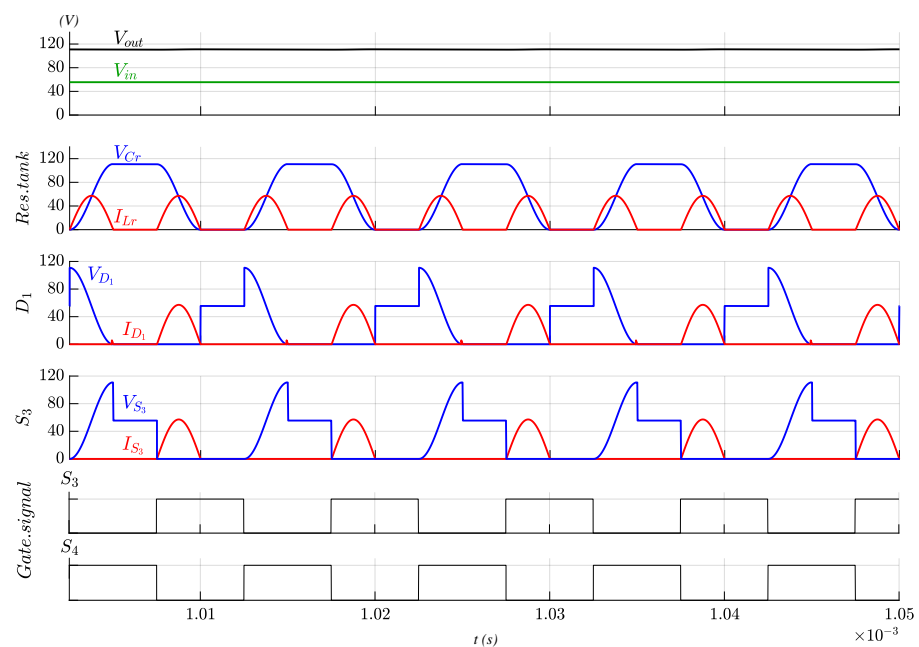

Figure 14. Boost simulation.

In Figure 14, the voltage and the current values of the resonant tank, one diode, and one switch are displayed. In the first one, the ability of the converter to reach V_{out} and the stability of the solution at the nominal operation of $G_{boost} = 2$ are reported. In the second one, the current through the resonant inductor and the voltage across the resonant capacitor are shown. The third and the forth display the current and voltage behavior through respectively diode D_1 and switch S_3. It is important to underline that there is no

overlapping of voltage and current for all the switching cycle operations. This means that in this ideal simulation, the switching losses are null and that the soft switching properties of the resonant converter are kept.

Figure 15 shows the buck simulation results. In buck operation, the waveforms of the voltage and current are plotted according to the switching signal. In this operation mode also, at turn-on and turn-off, the voltage and current waveforms of the switches have no overlap and the soft switching properties of the resonant converter are kept.

The behavior of the resonant tank is exactly the same as the boost analysis.

The simulation was performed at the maximum resonant gain $G_{buck} = 0.3$. As expected by the theoretical limitations, the charge and discharge times of the resonant inductor are equal to the semi-period. Therefore, this confirms the limitations of the resonant operations.
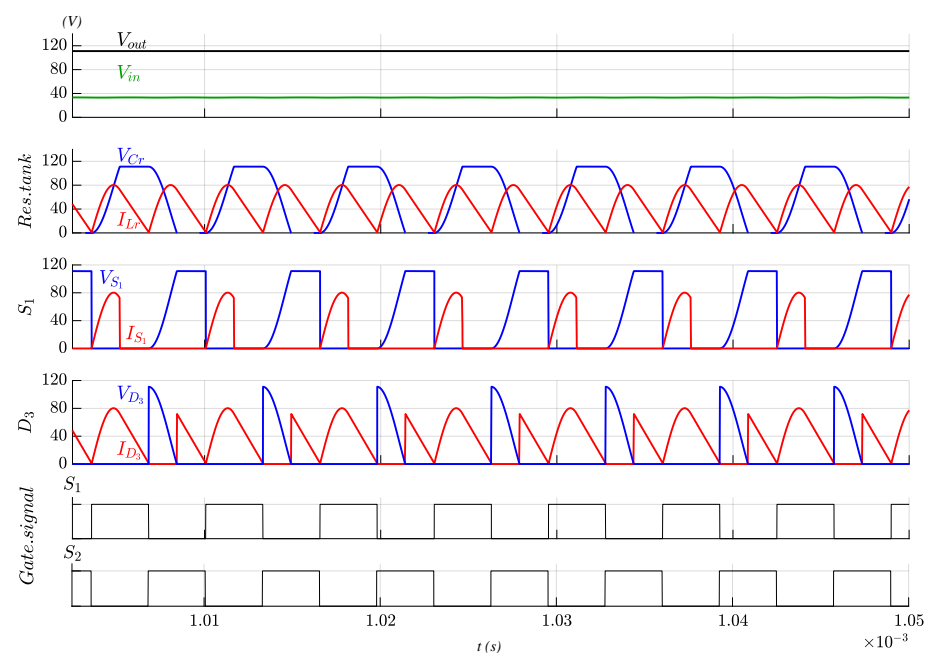

Figure 15. Buck simulation.

5. Conclusions

The analysis performed showed that the proposed electric vehicle is able to meet the requirements of the dynamical tests of the Formula SAE Electric competition. The simulation clearly confirms the correct sizing of the storage system with a good safety margin for real operation in which the prototype could exploit the full motor power. As expected, the Li-ion cells charge and discharge according to the theoretical implementation, complying with the current and voltage operational constraints on the inverter DC side. Instead, the KERS operation is strongly influenced by the state of charge of the UC pack that is disconnected under a certain voltage value to ensure the proper operation of the whole system.

The theoretical analysis of the resonant converter shows the full capability of the resonant converter to operate under soft-switching (ZCS) properties in both buck and boost operation while keeping the simplicity and a low count of the components. The limitations due to the high current EV application pushed the analysis to correctly sizing it. An inter-leaved solution combined with the introduction of the capability factor achieves the result of reducing both the peak current in the resonant inductor and both the input current to the UC pack. This converter can be easily paralleled, and the switches driving signals can be shifted, reducing current ripples at the input and output capacitor, as shown for the unidirectional boost [24] version. The findings suggest that the assumptions of the compactness

and low weight of the converter can be achieved and that the UC can co-work with the BP. Nonetheless, the converter is not able to fully exploit the peculiarities of the fast charge and discharge of the UC. Anyway, the ultracap technology implemented in the model remains an interesting asset to get the maximum advantage from regenerative braking.

Future works will deal with the development of a small-scale resonant converter prototype for experimental tests, as well as the study of solutions based on this converter topology, which will allow overcoming the issues related to the large peak current into the resonant tank inductor as compared to the average input current, making the converter even more suitable for an electric racing car.

References

1. World Energy Outlook 2018 (02–2019). Available online: https://www.iea.org/weo2018/ (accessed on 25 November 2020).
2. World Bank Data about Transport Emissions (02–2019). Available online: https://data.worldbank.org/indicator/EN.CO2.TRAN.ZS (accessed on 25 November 2020).
3. International Energy Agency Emission Statistics (02–2019). Available online: https://www.iea.org/statistics/co2emissions (accessed on 25 November 2020).
4. Formula SAE Electric Regulations (02–2019). Available online: https://www.fsaeonline.com/cdsweb/gen/DocumentResources.aspx(accessed on 25 November 2020).
5. Ehsani, M.; Gao, Y.; Gay, S.E.; Emadi, A. *Modern Electric, Hybrid Electric, and Fuel Cell Vehicles*; Chap. (2,4,6,10,11); CRC press: Boca Raton, FL, USA, 2018.
6. Mid-Eum, C.; Jun-Sik, L.; Seung-Woo, S. Real-Time Optimization for Power Management Systems of a Battery/Supercapacitor Hybrid Energy Storage System in Electric Vehicles. *IEEE Trans. Veh. Technol.* **2014**, *63*, 3600–3611.
7. Zhang, L.; Wang, Z.; Hu, X.; Sun, F.; Dorrell, D.G. A comparative study of equivalent circuit models of ultracapacitors for electric vehicles. *J. Power Sources* **2015**, *274*, 899–906. [CrossRef]
8. Zou, Z.; Cao, J.; Cao, B.; Chen, W. *Evaluation Strategy of Regenerative Braking Energy for Supercapacitor Vehicle*; ISA Transactions; Elsevier: Amsterdam, The Netherlands, 2015 ; Volume 55, pp. 234–240.
9. Radhika Kapoor, C.; Mallika P. Comparative Study on Various KERS. In Proceedings of the World Congress on Engineering 2013 Vol III, WCE 2013, London, UK, 3–5 July 2013.
10. Yu, Sh.; Chen, R.; Viswanathan, A. *Survey of Resonant Converter Topologies*; Reproduced from 2018 Texas Instruments Power Supply Design Seminar SEM2300© 2018; Texas Instruments Incorporated: Dallas, TX, USA, 2018.
11. Barbi, I.; Pöttker, F. *Soft Commutation Isolated DC-DC Converters*; Springer: Berlin/Heidelberg, Germany, 2019.
12. Zhang, Y.; Cheng, Xu.; Yin, C.; Cheng, S. A Soft-Switching Bidirectional DC-DC Converter for the Battery Super-Capacitor Hybrid Energy Storage System. *IEEE Trans. Ind. Electron.* **2018**, *65*, 7856–7865. [CrossRef]
13. Shuai, P.; De Novaes, Y.R.; Canales, F.; Barbi, I. A Non-Insulated Resonant Boost Converter. In Proceedings of the 2010 Twenty-Fifth Annual IEEE Applied Power Electronics Conference and Exposition (APEC), Palm Springs, CA, USA, 21–25 February 2010.
14. MATLAB and Simulink Racing Lounge: Vehicle Modeling. Available online: https://it.mathworks.com/matlabcentral/fileexchange/63823-matlab-and-simulink-racing-lounge-vehicle-modeling (accessed on 25 November 2020).
15. Morey, T.; Pressman, A.; Billing, K. *Switching Power Supply Design*, 3rd ed.; McGraw-Hill: New York, NY, USA, 2009.
16. Tabisz, W.A.; Jovanovic, M.M.; Lee, F.C. High-frequency multi-resonant converter technology and its applications. In Proceedings of the International Conference on Power Electronics and Variable Speed Drives, London, UK, 17–19 July 1990; pp. 1–8.
17. Med, M.; Tore, M.U.; William, P.R.*Power electronics: Converters, Applications and Design*, 2nd ed.; Chap. (2,9); John Wiley Sons: Hoboken, NJ, USA, 1995.
18. Hua, G.; Lee, F.C. An overview of soft-switching techniques for pwm converters. In Proceedings of the International Conference on Power Electronics and Motion Control, Beijing, China, 27–30 June 1994; pp. 801–808.
19. Rashid, M.H. *Power Electronics Handbook*; Chap. 15; Academic Press: Cambridge, MA, USA, 2001.
20. Lee, F.C. High-frequency quasi-resonant and multi-resonant converter technologies. In Proceedings of the 14 Annual Conference of Industrial Electronics Society, Singapore, 24–28 October 1988; pp. 509–521.
21. Robert, W. Erickson, Dragan Maksimovic. In *Fundamentals of Power Electronics*, 2nd ed.; Springer: Boston, MA, USA, 2001.

22. Orietti, E.; Mattavelli, P.; Spiazzi, G.; Adragna, C.; Gattavari, G. Two-phase interleaved LLC resonant converter with current-controlled inductor. In Proceedings of the Brazilian Power Electronics Conference, Bonito-Mato Grosso do Sul, Brazil, 27 September–1 October 2009.
23. Yi, J.H.; Choi, W.; Cho, B.H. Zero-Voltage-Transition Interleaved Boost Converter With an Auxiliary Coupled Inductor. *IEEE Trans. Power Electron.* **2017**, *32*, 5917–5930. [CrossRef]
24. Shuai, P. *Investigation of a Non-insulated Resonant Converter for Power Processing of Alternative Energy Sources*; Institute for Power Electronics and Electrical Drives (ISEA) RWTH-Aachen University: Aachen, Germany, 2009.